Interface-Confined Ferrous Centers for Catalytic Oxidation

Qiang Fu *et al.*

Science **328**, 1141 (2010);
DOI: 10.1126/science.1188267

Science (print ISSN 0036-8075; online ISSN 1095-9203) is published weekly, except the last week in December, by the American Association for the Advancement of Science, 1200 New York Avenue NW, Washington, DC 20005.

24. E. Rabkin, *J. Mater. Sci.* **40**, 875 (2005).
25. M. Anderson, G. Grest, D. Srolovitz, *Philos. Mag. B* **59**, 293 (1989).
26. M. Anderson, D. Srolovitz, G. Grest, P. Sahni, *Acta Metall.* **32**, 783 (1984).
27. G. N. Hassold, E. Holm, *Comput. Phys.* **7**, 97 (1993).
28. Materials and methods are available as supporting material on *Science* Online.
29. M. Hillert, *Acta Metall.* **36**, 3177 (1988).
30. P. Hazzledine, R. Oldershaw, *Philos. Mag. A* **61**, 579 (1990).
31. S. M. Foiles, J. J. Hoyt, *Acta Mater.* **54**, 3351 (2006).
32. S. J. Plimpton, LAMMPS Molecular Dynamics Simulator (Sandia National Laboratories, Albuquerque, NM, 2007), http://lammps.sandia.gov.
33. A. Galina, V. Fradkov, L. Schvindlerman, *Fiz. Met. Metalloved.* **63**, 1220 (1987).
34. D. Farkas, S. Mohanty, J. Monk, *Phys. Rev. Lett.* **98**, 165502 (2007).
35. Our initial work on grain growth with frozen boundaries, which informed this study, was performed in collaboration with G. Hassold. Support for this work was provided by the U.S. Department of Energy (DOE), Office of Basic Energy Sciences, and by the Laboratory Directed Research and Development program at Sandia National Laboratories. Sandia National Laboratories is a multiprogram laboratory operated by Sandia Corporation, a wholly owned subsidiary of Lockheed Martin company, for the DOE's National Nuclear Security Administration under contract DE-AC04-94AL85000.

Supporting Online Material

www.sciencemag.org/cgi/content/full/328/5982/1138/DC1
Materials and Methods
References and Notes

2 February 2010; accepted 19 April 2010
10.1126/science.1187833

Interface-Confined Ferrous Centers for Catalytic Oxidation

Qiang Fu,[1]* Wei-Xue Li,[1,2]* Yunxi Yao,[1] Hongyang Liu,[1] Hai-Yan Su,[1,2] Ding Ma,[1] Xiang-Kui Gu,[1,2] Limin Chen,[1] Zhen Wang,[1] Hui Zhang,[3] Bing Wang,[3] Xinhe Bao[1]†

Coordinatively unsaturated ferrous (CUF) sites confined in nanosized matrices are active centers in a wide range of enzyme and homogeneous catalytic reactions. Preparation of the analogous active sites at supported catalysts is of great importance in heterogeneous catalysis but remains a challenge. On the basis of surface science measurements and density functional calculations, we show that the interface confinement effect can be used to stabilize the CUF sites by taking advantage of strong adhesion between ferrous oxides and metal substrates. The interface-confined CUF sites together with the metal supports are active for dioxygen activation, producing reactive dissociated oxygen atoms. We show that the structural ensemble was highly efficient for carbon monoxide oxidation at low temperature under typical operating conditions of a proton-exchange membrane fuel cell.

In many catalytic processes, the size of metal-containing catalysts falls typically in the range of 1 to 10 nm. The catalytically active sites in these catalysts are often coordinatively unsaturated metal cations that are able to undergo facile electron transfer and promote catalytic reactions, as has been studied in (*1*–*5*). In oxygen-carrying hemoglobin, the iron (II) ion constrained in a planar porphyrin ring could transport O_2 via facile interconversion between Fe^{2+} and Fe^{3+} states (*6*). Homogeneous catalysis in aqueous solutions uses Fenton's reagent, being a mixture of Fe^{2+} ions and H_2O_2, to produce hydrated ferryl ions $[(H_2O)_5Fe^{IV}O]^{2+}$, which act as the active intermediates to oxidize various organic compounds, such as methane (*7*). However, for heterogeneous catalysis with nanopore environments the active species in Fe-ZSM-5 and Fe-silicalite zeolites are also coordinatively unsaturated Fe^{2+} grafted to the zeolite crystalline matrix. The dissociation of N_2O at the Fe sites leads to formation of "α-oxygen" species, which are active in the selective oxidation of benzene to phenol at mild conditions (*8*). These characteristic coordinatively unsaturated ferrous (CUF) sites are confined by various ensembles such as proteins, ligands, and nanopore matrix, which are essential for their high reactivity and stability in the catalytic oxidation reactions mentioned above (*9*).

Preparation of an analogous ensemble at supported heterogeneous catalysts, which account for 80% of the catalytic processes in industrial chemistry, is of great importance. This, however, remains a challenge because of their high structural complexity and flexibility under operating conditions. On the basis of surface science measurements, density functional calculations, and catalytic reactions under realistic conditions, we describe here a strategy to achieve this goal that takes advantage of the confinement effect at interfaces between nanostructured ferrous oxides (FeO) and metal (Pt) substrates. The interface-confined CUF sites and neighboring Pt atoms are identified conclusively as the active centers to activate O_2. The dissociated atomic oxygen atoms therein present modest adsorption energy and thus are highly reactive. Catalytic reaction experiments on the supported Pt-Fe catalysts prepared by a dedicated and reproducible synthesis method show that the identified ensemble is highly active, selective, and robust for CO oxidation, even under operating conditions of a proton-exchange membrane fuel cell (PEMFC).

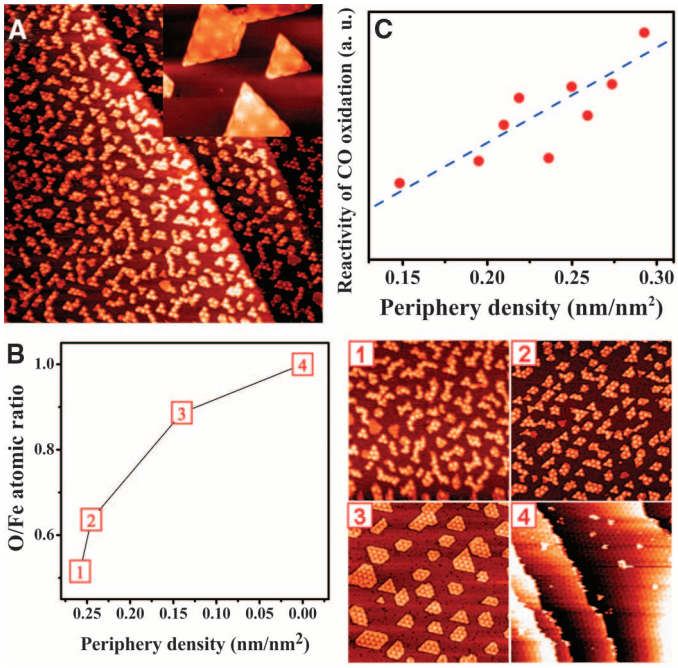

Fig. 1. (**A**) STM image (200 nm × 200 nm) from the 0.25-ML FeO_{1-x}/Pt(111) surface. (Inset) An atomic-resolution STM image of FeO monolayer nanoislands (25 nm × 20.8 nm) recorded at liquid N_2 temperature. (**B**) Ratios of XPS O 1*s* to Fe $2p_{3/2}$ peak intensity from FeO_{1-x}/Pt(111) surfaces with different periphery density of FeO nanoisland. Samples 1 to 3 are 0.25-ML FeO nanoislands prepared at 1.3 × 10^{-6} mbar O_2 and annealed in UHV at 473, 573, and 673 K, respectively. Sample 4 is the full-monolayer FeO film on Pt(111). The STM images are all 100 nm by 100 nm. (**C**) Dependence of reactivity of CO oxidation on the periphery density at 0.25-ML FeO_{1-x}/Pt(111) surfaces.

[1]State Key Laboratory of Catalysis, Dalian Institute of Chemical Physics, Chinese Academy of Sciences, Dalian 116023, China. [2]Center for Theoretical and Computational Chemistry, Dalian Institute of Chemical Physics, Chinese Academy of Sciences, Dalian 116023, China. [3]Hefei National Laboratory for Physical Sciences at the Microscale, University of Science and Technology of China, Hefei 230026, China.

*These authors contributed equally to this work.
†To whom correspondence should be addressed. E-mail: xhbao@dicp.ac.cn

Construction of FeO nanoislands on the metal support was done by depositing Fe on Pt(111) under oxidizing conditions and characterized by an ultra-high vacuum (UHV) multi-probe surface system (*10*). Figure 1A shows a typical scanning tunneling microscopy (STM) image taken from Pt(111) with 0.25-monolayer (ML) Fe deposited at 150 K in the presence of 1.3×10^{-7} mbar O_2, followed by annealing up to 473 K in UHV. The FeO nanoislands formed are monolayer-dispersed. The Moiré patterns and surface atomic structures of the nanoislands are the same as those of a monolayer FeO film grown on Pt(111), comprising one layer of Fe above Pt substrates and one layer of O on top of the Fe layer (*11*). The presence of ferrous species was further verified by the characteristic x-ray photoelectron spectra (XPS) Fe $2p_{3/2}$ peak at binding energy (BE) of 709.3 eV, in comparison with the BEs of 707.3 eV from a metallic Fe film grown on Pt(111) and 711.0 eV in ferric oxide deposited on highly oriented pyrolytic graphite (fig. S1).

At the periphery of the two-dimensional (2D) FeO nanoislands, there are a number of CUF sites indicated by the decreased ratio of the measured O 1s and Fe $2p_{3/2}$ peak heights as compared with that of the monolayer FeO films grown on Pt(111). To more easily identify the changes, we deposited a fixed amount of Fe (0.25 ML) but annealed at various temperatures. In this way, the corresponding dispersion of FeO nanoislands prepared could be changed gradually. To quantify the dispersion, we defined the specific periphery density (SPD) as the length of the periphery of FeO nanoislands per unit area of the Pt substrate. As shown in Fig. 1B, the ratios of O/Fe XPS signals measured from 0.25 ML FeO nanoislands with different dispersions are all less than that of the monolayer stoichiometric FeO film on Pt(111). This shows that the FeO nanoislands are oxygen-deficient. Moreover, the ratio of O/Fe XPS signals decreases monotonically as the SPD increases. This means that the oxygen deficiency mainly occurs at the peripheries of FeO nanoislands, and the corresponding ferrous Fe atoms there are coordinatively unsaturated (denoted as FeO_{1-x}/Pt(111), $x < 1$).

XPS and ultraviolet photoelectron spectroscopy (UPS) were used to study CO oxidation on the 0.25 ML FeO_{1-x}/Pt(111) surfaces. Because of the strong bonding of CO on Pt (*12*), the exposed Pt(111) surface would be saturated by CO even at room temperature (RT). In contrast, the FeO surface is inert for CO adsorption at RT (*13*). This can be seen from fig. S2, in which the O 1s peak from the adsorbed CO decreases linearly with the coverage of the FeO nanoislands. To investigate the reactivity of the FeO_{1-x}/Pt(111) surfaces, we first presaturated the samples with CO. Afterward, a steady-state flux of O_2 at nominally 5.2×10^{-8} mbar was leaked into the chamber at RT. The removal of CO was studied by monitoring the variation of the characteristic in situ UPS peaks at a BE of 9.4 eV from 5σ and 1π states of adsorbed CO (*14*). On the FeO_{1-x}/Pt(111) surfaces, the adsorbed CO was found to react off by O_2 exposure within 5 min, whereas Pt(111) shows negligible activity under the same conditions. The reaction rate was determined on the basis of the UPS intensity versus the reaction time plots (fig. S3). In Fig. 1C, the rate of CO removal is plotted as a function of the SPD of the FeO nanoislands, and a linear correlation between the rate and SPD can be seen. This shows unambiguously that the CUF sites at the peripheries of the FeO nanoislands on Pt(111) are the active sites for CO oxidation.

If the prepared 2D FeO nanoislands were oxidized further (to 1.3×10^{-6} mbar O_2, 673 K) to 3D ferric oxide nanoislands [denoted as FeO_{1+x}/Pt(111)], the corresponding reactivity was remarkably lower at RT (fig. S4). Considerable reactivity could only be found when the temperature was higher than 400 K (*15*). The reactivities of metallic Fe overlayers grown on Pt(111) and Pt(111) with subsurface Fe were lowered too (fig. S4). Among various model systems considered, the FeO_{1-x}/Pt(111) surface presents the highest reactivity because of the presence of the CUF sites.

Density functional theory (DFT) calculations were performed in order to reveal the origin of the high reactivity of the FeO_{1-x}/Pt(111) surfaces (*10*). First, calculated adsorption energies for CO and O_2 on Pt(111) (0.25 ML) are –1.64 eV per CO molecule and –0.71 eV per O_2 molecule (Fig. 2A). The substantially larger adsorption energy of CO than O_2 by about one eV indicates that Pt(111) tends to be covered by CO, which would block the sites for O_2 adsorption and activation. Thus, CO oxidation on Pt(111) would be hindered by adsorbed CO at modest temperatures despite that the calculated reaction barrier (0.85 eV) between CO and dissociated O is not high, which agrees well with previous experiments (*16*).

In contrast, FeO_{1-x}/Pt(111) shows a much higher reactivity for O_2 activation (fig. S5). Depending on the CUF sites, O_2 may either dissociate directly to atomic O without barrier, or adsorb molecularly first with a binding energy of about –1.51 eV per O_2 (Fig. 2A) and afterward dissociate to atomic O with a barrier of 0.42 eV [the corresponding transition state (TS) shown in Fig. 2B]. On the other hand, we find that CO adsorption at the CUF sites is unstable. The preferential adsorption and activation of O_2 over the CUF sites on the FeO_{1-x}/Pt(111) surfaces are the main reason why these surfaces do not become CO poisoned. Adsorption energy for the dissociated O atoms at the CUF sites is –1.10 eV/O. Compared with oxygen atoms adsorbed on metallic Fe or inside a 2D FeO overlayer with energy of –3.0 eV, which was too strong to be reactive, the bonding strength for

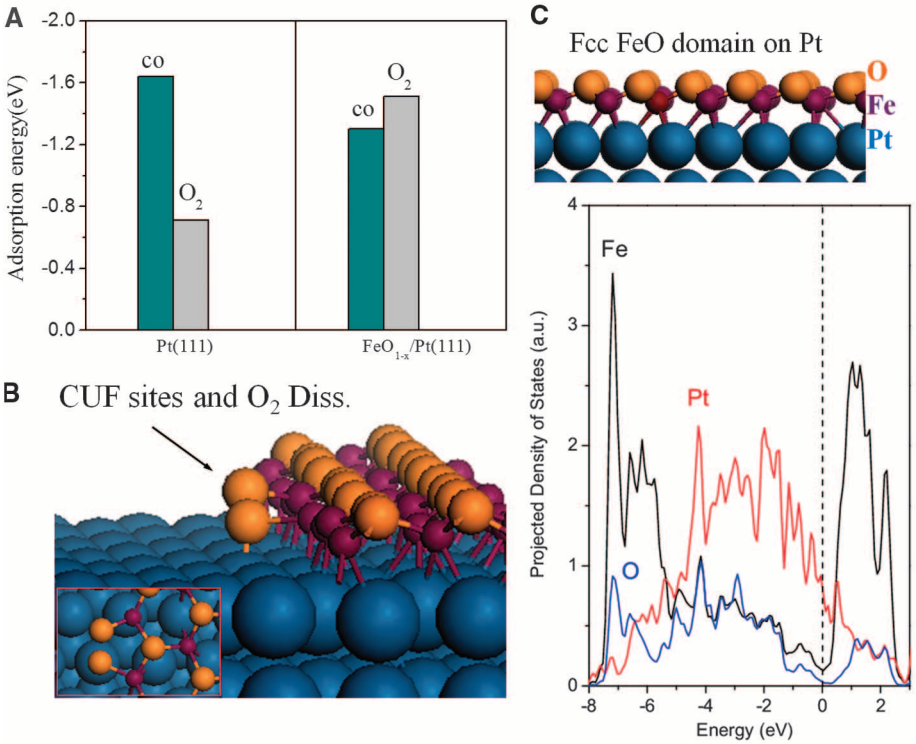

Fig. 2. (**A**) Calculated adsorption energy (in eV) for CO and O_2 molecules on Pt(111) and FeO_{1-x}/Pt(111) surfaces. (**B**) Schematic structure of the CUF sites and calculated transition states of O_2 dissociation (the inset shows the top view) at the boundary between FeO and Pt(111). (**C**) Projected density of states for interfacial Fe, O, and Pt atoms at FCC domains of FeO overalyer on Pt(111) using $(\sqrt{84} \times \sqrt{84})R10.9^0$–FeO/Pt(111) supercell. Pt, Fe, C, and O atoms are indicated by blue, purple, gray, and brown balls, respectively. For details, see figs. S5, S6, and S7 and (*10*).

O atoms at the CUF sites is optimum and would make these sites active. Indeed, the reaction barrier between O at the CUF sites and CO adsorbed on neighboring Pt atoms is only 0.63 eV (the corresponding TS is shown in fig. S6). After removal of atomic O by CO, Fe atoms at the boundary resume the coordinatively unsaturated state and get ready for O_2 adsorption and dissociation to close the cycle. In this catalytic cycle, the boundary between the FeO nanoisland and Pt provides multiple sites (CUF and Pt atoms) for O_2 activation and CO adsorption, and the CO oxidation occurs according to the bifunctional mechanism (*17*, *18*).

The formation of the CUF sites at the peripheries of the FeO nanoislands is due to the stabilization of interface confinement between the oxide overlayers and the metal supports. To verify this, we studied the interfacial interaction between FeO overlayer and Pt(111) substrate using a model of $(\sqrt{84} \times \sqrt{84})R10.9^0$ – FeO/Pt(111), and the calculated interfacial adhesion energy is 1.40 eV per FeO formula (fig. S7). The interfacial adhesion comes from the strong interaction between interfacial Fe and Pt atoms, as seen clearly from their extensive orbital hybridizations (Fig. 2C). The strong adhesion between FeO overlayers and Pt substrates stabilizes the monolayer ferrous oxide against further oxidation into ferric oxide (*19*, *20*). CO oxidation on FeO_{1-x}/Pt(111) might maintain its activity even in the presence of H_2 because dissociative adsorption of H_2 on Pt suffers from CO poisoning. Indeed, our calculations show that on 0.67-ML CO precovered Pt(111), dissociative adsorption of H_2 becomes endothermic. Meanwhile, dissociative adsorption of H_2 on FeO at RT is difficult, too (*21*, *22*). This is desirable for the preferential oxidation of CO in excess of H_2 (PROX) (*18*, *23*, *24*).

Guided by these insights, we prepared Pt-Fe [4 weight percent (wt %) Pt, 0.5 wt % Fe] nanoparticles (NPs) and Pt (4 wt %) NPs supported on nanosized silica spheres. To realize the main structural features shown above, we developed a dedicated preparation process with proper reduction at 473 K for 2 hours in H_2 (*10*). The treatment with H_2 reduces the as-prepared samples to metallic states. Transmission electron microscopy (TEM) analysis found that the metal NPs in the Pt/SiO_2 (Fig. 3A) and Pt-Fe/SiO_2 (Fig. 3B) samples are anchored evenly over the silica hosts and have a narrow distribution in average size of 2 to 3 nm and 2 to 4 nm, respectively. High-resolution TEM (HRTEM) images (Fig. 3, A and B, insets) show that NPs over both Pt/SiO_2 and Pt-Fe/SiO_2 samples present the same face-centered cubic (FCC) Pt lattice with a Pt(111) interlayer spacing of 0.23 nm. This means that the cores of the Pt-Fe NPs are still dominated by Pt. This was further corroborated through x-ray diffraction (XRD) measurements. There is no shift of 2θ value for the Pt-Fe NPs compared to the Pt/SiO_2 sample observed (fig. S8), and the formation of PtFe bulk alloy in the Pt-Fe NPs is excluded. We performed an energy-dispersive x-ray spectroscopic (EDX) mapping and point analysis over dozens of the Pt-Fe NPs, and found that Fe signal is accompanied exclusively with Pt signal (fig. S9). These show that Fe species are present mainly on the outer layers of the Pt-Fe NPs. However, Fe does not completely cover Pt-Fe NPs because there is a considerable amount of CO adsorbed on Pt-Fe/SiO_2 samples, as seen from temperature-programmed desorption (TPD) experiments (fig. S10). Correspondingly, the structure of the prepared Pt-Fe NPs consists of the Pt NPs with Fe patches on the surfaces.

CO PROX reactions under stoichiometric condition (1% CO and 0.5% O_2, 98.5% H_2, 0.1 M Pa, 36000 ml g^{-1} h^{-1}) are conducted on the Pt-Fe/SiO_2 and Pt/SiO_2 catalysts. The corresponding activity and selectivity were measured from the temperature-dependent reaction profiles (Fig. 3, C and D). For the Pt/SiO_2 catalysts, CO conversion is negligible below RT, but increases slowly with temperature. At 473 K, only 70% CO was reacted off. In contrast, the Pt-Fe/SiO_2 catalysts show a high activity, with almost 100% CO conversion and 100% CO selectivity at RT. At 353 K, the catalysts have 95% CO conversion and 95% selectivity, which remain high. Even at 200 K, the Pt-Fe/SiO_2 catalysts maintain 20% CO conversion and 100% CO selectivity. We measured the oxidation state of the Fe species under reaction conditions using in situ x-ray adsorption spectroscopy (XAFS) performed in the beamline of BL14W1 in the Shanghai Synchrotron Radiation Facility (SSRF) (fig. S11). Compared with the Fe K-edge XAFS spectra from the reduced and fully oxidized Pt-Fe catalysts, the pre-edge feature from the Pt-Fe NPs under the reaction conditions was located in the middle. This shows the presence of ferrous species under the operating conditions. Thus, the highly active Pt-Fe NPs in the CO PROX reaction should comprise Pt-rich core and ferrous species on the surfaces, restoring the characteristics of the FeO_{1-x}/Pt(111) model system described in the above model system.

The Pt-Fe catalysts prepared are very stable, and no deterioration of their performance was found after 40 hours at RT (fig. S12). Under PEMFC working conditions operated typically at 353 to 373 K, there are considerable amounts of water and CO_2 present. We tested the Pt-Fe catalysts under the realistic PEMFC conditions. As plotted in fig. S13, the catalysts were stable and showed good performances, with 92% CO selectivity/conversion at 353 K. By using slight excess of O_2, CO can be removed to a level lower than 1 part per million (fig S14). We also assembled the Pt-Fe nanocatalysts into a 1-kW PEMFC working system. We found that the cell performance stays quite stable after a 930-hour test but deactivates quickly after a 30-min test without using the Pt-Fe catalyst (fig. S15). Extraordinary activity and stability of the Pt-Fe catalysts under the operating conditions suggests that the Pt-Fe nanocatalysts prepared are eligible for industrial applications.

We demonstrated a strategy of preparing coordinatively unsaturated metal sites with lower valent states on metal substrates by taking advantage of the confinement effects at interfaces between nanostructured oxides and metal substrates. The confined CUF sites and neighboring metal atoms show a high activity and stability in CO oxidation under realistic conditions. The concept of interface confinement and fabrication of coordinately unsaturated low-valent cations

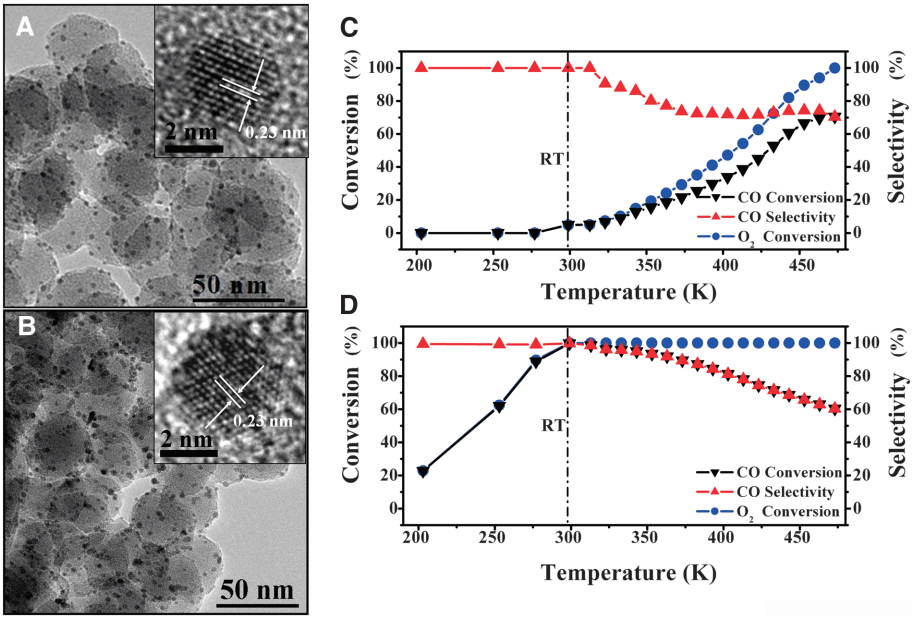

Fig. 3. TEM images of the (**A**) Pt/SiO_2 and (**B**) Pt-Fe/SiO_2 catalysts pretreated with H_2 at 473 K for 2 hours. Insets show HRTEM images. (**C** and **D**) PROX reaction of the (C) Pt/SiO_2 and (D) Pt-Fe/SiO_2 catalysts under the conditions 1% CO, 0.5% O_2, and 98.5% H_2. Space velocity is 36000 ml $g^{-1}h^{-1}$; pressure = 0.1 MPa.

could be widely applied in various heterogeneous oxides-metals catalytic systems and illustrates a promising and efficient way to design active sites for nanocatalysts.

References and Notes

1. G. A. Somorjai, J. Y. Park, *Angew. Chem. Int. Ed.* **47**, 9212 (2008).
2. K. Honkala *et al.*, *Science* **307**, 555 (2005).
3. J. H. Kwak *et al.*, *Science* **325**, 1670 (2009).
4. J. M. Thomas, *J. Chem. Phys.* **128**, 182502 (2008).
5. T. F. Jaramillo *et al.*, *Science* **317**, 100 (2007).
6. T. K. Das, M. Couture, Y. Ouellet, M. Guertin, D. L. Rousseau, *Proc. Natl. Acad. Sci. U.S.A.* **98**, 479 (2001).
7. B. Ensing, F. Buda, M. C. M. Gribnau, E. J. Baerends, *J. Am. Chem. Soc.* **126**, 4355 (2004).
8. G. I. Panov, A. K. Uriarte, M. A. Rodkin, V. I. Sobolev, *Catal. Today* **41**, 365 (1998).
9. A. Zecchina, M. Rivallan, G. Berlier, C. Lamberti, G. Ricchiardi, *Phys. Chem. Chem. Phys.* **9**, 3483 (2007).
10. Materials and methods are available as supporting material on *Science* Online.
11. W. Weiss, W. Ranke, *Prog. Surf. Sci.* **70**, 1 (2002).
12. Y. Y. Yeo, L. Vattuone, D. A. King, *J. Chem. Phys.* **106**, 392 (1997).
13. R. Meyer *et al.*, *Surf. Sci.* **586**, 174 (2005).
14. T. Ma *et al.*, *ChemPhysChem* **10**, 1013 (2009).
15. Y. N. Sun *et al.*, *J. Catal.* **266**, 359 (2009).
16. C. Campbell, G. Ertl, H. Kuipers, J. Segner, *J. Chem. Phys.* **73**, 5862 (1980).
17. J. A. Rodriguez *et al.*, *Science* **318**, 1757 (2007).
18. M. Kotobuki, A. Watanabe, H. Uchida, H. Yamashita, M. Watanabe, *J. Catal.* **236**, 262 (2005).
19. Q. Fu, T. Wagner, *Surf. Sci. Rep.* **62**, 431 (2007).
20. F. P. Netzer, *Surf. Rev. Lett.* **9**, 1553 (2002).
21. L. R. Merte *et al.*, *Surf. Sci.* **603**, L15 (2009).
22. W. X. Huang, W. Ranke, *Surf. Sci.* **600**, 793 (2006).
23. X. S. Liu, O. Korotkikh, R. Farrauto, *Appl. Catal. A Gen.* **226**, 293 (2002).
24. S. Alayoglu, A. U. Nilekar, M. Mavrikakis, B. Eichhorn, *Nat. Mater.* **7**, 333 (2008).

25. We gratefully acknowledge the Natural Science Foundation of China, Chinese Academy of Sciences, and Ministry of Science and Technology of China for the support of this work. We thank the SSRF and Sunrise Power Co. for the beamline and assistance with the PEMFC test.

Supporting Online Material

www.sciencemag.org/cgi/content/full/328/5982/1141/DC1
Materials and Methods
Figs. S1 to S15
References

12 February 2010; accepted 19 April 2010
10.1126/science.1188267

Self-Assembled $M_{24}L_{48}$ Polyhedra and Their Sharp Structural Switch upon Subtle Ligand Variation

Qing-Fu Sun,[1] Junji Iwasa,[1] Daichi Ogawa,[1] Yoshitaka Ishido,[1] Sota Sato,[1] Tomoji Ozeki,[2] Yoshihisa Sei,[3] Kentaro Yamaguchi,[3] Makoto Fujita[1]*

Self-assembly is a powerful technique for the bottom-up construction of discrete, well-defined nanoscale structures. Large multicomponent systems (with more than 50 components) offer mechanistic insights into biological assembly but present daunting synthetic challenges. Here we report the self-assembly of giant $M_{24}L_{48}$ coordination spheres from 24 palladium ions (M) and 48 curved bridging ligands (L). The structure of this multicomponent system is highly sensitive to the geometry of the bent ligands. Even a slight change in the ligand bend angle critically switches the final structure observed across the entire ensemble of building blocks between $M_{24}L_{48}$ and $M_{12}L_{24}$ coordination spheres. The amplification of this small initial difference into an incommensurable difference in the resultant structures is a key mark of emergent behavior.

Chemists are often inspired by the spontaneous and precise assembly of multiple protein subunits into giant, well-defined, functional superstructures (*1*, *2*). Spherical virus capsids, consisting of hundreds to thousands of identical protein subunits, are simple and accessible examples of biological self-assembly and have been extensively studied (*3*, *4*) and mimicked on a much smaller scale. Most virus capsids are polyhedra assembled from 60*T* subunits, where *T* is a mathematically defined triangulation number, and *T* = 1, 3, 4, 7, 13, and 16 are naturally occurring values (*5*, *6*). As a result, the possible final capsid polyhedral structures are limited by simple geometrical constraints.

Similar geometrical constraints have often been used in artificial multicomponent self-assembly (*7*–*26*). The formation of roughly spherical polyhedra with a general formula of M_nL_{2n} is predicted when metal ions with square planar coordination sphere (M) and rigid bent ligands (L) are mapped onto the vertices and edges, respectively, of the polyhedra. For entropically favored regular or semiregular polyhedra, *n* is limited by geometrical constraints to be 6, 12, 24, 30, or 60 (Fig. 1A) (*27*), and spherical coordination assemblies have been reported for *n* = 6 (*25*) and 12 (*10*, *26*) but not for larger *n* values. Here we report the self-assembly of the giant, 5-nm-diameter $M_{24}L_{48}$ spherical framework **2** (where *n* = 24) from square planar Pd^{2+} ions and bent dipyridylthiophene ligand **1** (Fig. 1B). The formation of this 72-component system is highly sensitive to the ligand geometry. We previously reported that the smaller 36-component $M_{12}L_{24}$ coordination sphere **4** (*n* = 12) forms when the analogous dipyridylfuran ligand **3** is used (Fig. 1C) (*10*). Systematically varying the mean ligand angle by mixing **1** and **3** in various ratios revealed that even a slight change in the mean ligand bend angle critically switches the final structure between $M_{24}L_{48}$ and $M_{12}L_{24}$ coordination spheres. The amplification of a small initial difference into an incommensurable difference in the resultant structures is a key mark of emergent behavior. Emergent phenomena are attracting considerable current interest (*28*–*30*) and usually refer to the emergence of macroscopic differences based on microscopic differences. We believe that our results are a good example of chemical emergence because an incommensurable difference is observed at a molecular level. By demonstrating, in an artificial system, emergent behavior on similar scale to that observed in the assembly of biological structures, we provide a synthetically simple system for the mechanistic scrutiny of massive multicomponent self-assembly. In addition, we extend the scale and the practical feasibility of using self-assembly as a powerful bottom-up technology for the construction of discrete nanoscale systems.

Ligands **1a** to **1c** were synthesized in a single step from 4-pyridyl pinacol boronate ester and the corresponding 2,5-dihalothiophenes in reasonable yields by using the Suzuki-Miyaura procedure (*31*). When ligand **1a** (10 μmol) and $Pd(NO_3)_2$ (5.0 μmol) were heated in dimethyl sulfoxide-d_6 (DMSO-d_6) (0.7 ml) at 70°C for 17 hours, two broad peaks were observed in the ^{1}H nuclear magnetic resonance (NMR) spectrum (Fig. 2B). The peak at 9.2 parts per million (ppm) was assigned to PyH_α (Py = pyridyl) and the peak at 8.0 ppm was assigned to the superimposed PyH_β and thiophene protons, where α and β indicate the two positions on the pyridinyl group. The broad ^{1}H and ^{13}C signals are indicative of a very large complex, the tumbling motion of which is slow on the NMR time scale. Diffusion-ordered NMR spectroscopy (DOSY) evinced a single product with a single band at diffusion coefficient $D = 3.3 \times 10^{-11}$ m^2•s^{-1} (log$D$ = –10.49) (Fig. 2C), which is indicative of a much larger structure than $M_{12}L_{24}$ coordination sphere **4**, which has a log$D$ value of –10.3. A quantitative yield was confirmed by ^{1}H (one-dimensional and DOSY) and ^{13}C NMR spectra and mass spectrometry (MS). The coordination of ligands **1b** and **1c** with

[1]Department of Applied Chemistry, School of Engineering, The University of Tokyo and Core Research for Evolutional Science and Technology (CREST), Japan Science and Technology Corporation (JST), 7-3-1 Hongo, Bunkyo-ku, Tokyo 113-8656, Japan. [2]Department of Chemistry and Materials Science, Tokyo Institute of Technology, 2-12-1 O-okayama, Meguro-ku, Tokyo 152-8551, Japan. [3]Faculty of Pharmaceutical Sciences at Kagawa Campus, Tokushima Bunri University, 1314-1 Shido, Sanuki, Kagawa 769-2193, Japan.

*To whom correspondence should be addressed. E-mail: mfujita@appchem.t.u-tokyo.ac.jp